



Article

# Mapping Large-Scale Mangroves along the Maritime Silk Road from 1990 to 2015 Using a Novel Deep Learning Model and Landsat Data

Yujuan Guo <sup>1,2</sup> , Jingjuan Liao <sup>1,3,\*</sup> and Guozhuang Shen <sup>1</sup>

<sup>1</sup> Key Laboratory of Digital Earth Science, Aerospace Information Research Institution, Chinese Academy of Sciences, Beijing 100094, China; guoyj@radi.ac.cn (Y.G.); shengz@radi.ac.cn (G.S.)

<sup>2</sup> University of Chinese Academy of Sciences, Beijing 100049, China

<sup>3</sup> Key Laboratory of Earth Observation, Sanya 572000, China

\* Correspondence: liaojj@ircas.ac.cn

**Abstract:** Mangroves are important ecosystems and their distribution and dynamics can provide an understanding of the processes of ecological change. Meanwhile, mangroves protection is also an important element of the Maritime Silk Road (MSR) Cooperation Project. Large amounts of accessible satellite remote sensing data can provide timely and accurate information on the dynamics of mangroves, offering significant advantages in space, time, and characterization. In view of the capability of deep learning in processing massive data in recent years, we developed a new deep learning model—Capsules-Unet, which introduces the capsule concept into U-net to extract mangroves with high accuracy by learning the spatial relationship between objects in images. This model can significantly reduce the number of network parameters to improve the efficiency of data processing. This study uses Landsat data combined with Capsules-Unet to map the dynamics of mangrove changes over the 25 years (1990–2015) along the MSR. The results show that there was a loss in the mangrove area of 1,356,686 ha (about 21.5%) between 1990 and 2015, with anthropic activities such as agriculture, aquaculture, tourism, urban development, and over-development appearing to be the likely drivers of this decline. This information contributes to the understanding of ecological conditions, variability characteristics, and influencing factors along the MSR.



**Citation:** Guo, Y.; Liao, J.; Shen, G. Mapping Large-Scale Mangroves along the Maritime Silk Road from 1990 to 2015 Using a Novel Deep Learning Model and Landsat Data. *Remote Sens.* **2021**, *13*, 245. <https://doi.org/10.3390/rs13020245>

Received: 2 December 2020

Accepted: 10 January 2021

Published: 13 January 2021

**Publisher's Note:** MDPI stays neutral with regard to jurisdictional claims in published maps and institutional affiliations.



**Copyright:** © 2021 by the authors. Licensee MDPI, Basel, Switzerland. This article is an open access article distributed under the terms and conditions of the Creative Commons Attribution (CC BY) license (<https://creativecommons.org/licenses/by/4.0/>).

## 1. Introduction

Mangroves are distributed along tropical and subtropical coastlines between 32°N and 38°S [1]. These forests play an important role in terms of ecological functions (e.g., coastal protection [2], carbon sinks [3], and biodiversity conservation [4]) in addition to providing a wide range of ecosystem services for tens of millions of people [5,6]. However, nearly one-third of the world's mangroves have disappeared over the past 50 years [7] and they are still declining at an annual rate of 1–2% [8,9]. Mangroves are threatened by both natural (e.g., sea level rise [10], hurricanes [11], and precipitation intensity [12]) and anthropogenic forces (e.g., aquaculture [13], urban development [14], and timber harvesting [15]). They face challenges in terms of area loss, functional degradation, and distribution fragmentation [16], thereby threatening the resilience and viability of coastal socio-ecological systems around the world.

Environmental protection is one of the key areas of cooperation in the construction of the Maritime Silk Road (MSR). Indonesia alone accounted for 22.6% of the global mangrove area in 2001 [17]. Sundarbans, located on the India-Bangladesh border, covers approximately 1,000,000 ha and has the largest mangrove ecosystem in the world [18]. Mangrove species diversity along the MSR varies significantly. Southeast Asia, with 51 of the world's 73 known species, is the center of mangrove diversity [17,19]. The MRS is characterized

by complex ecological conditions and frequent land cover conversions. As important and sensitive ecological indicators, mangroves are monitored and analyzed to help understand the process of ecological change along the MSR. Therefore, accurate and timely information on the distribution of mangroves along the MSR is essential for mangrove mapping, change detection, biomass estimation, and sustainable mangrove management.

Remote sensing technology has advantages in terms of large observation scale, high data timeliness, and few restrictions by ground conditions; it can be leveraged to efficiently and accurately obtain information on mangroves distribution and spatial and temporal changes [20,21]. In recent years, the availability of remote sensing data, advanced image processing methods, and the development of computational and information technologies have provided an attractive option for continuous observation of mangroves on a large scale [22,23]. For example, Cavanaugh et al. evaluated the sensitivity of mangroves to climate change by calculating the enhanced vegetation index (EVI) from 1984 to 2011 [24]; Liao et al. used multi-temporal Landsat data to map the 30-year change in mangrove distribution on Hainan Island of China [25]. Mangroves have very distinct spectral characteristics in remote sensing data, especially in the near-infrared band with strong reflectivity. It is common practice to identify mangroves by calculating band indices [26–28] or designing classifiers [29,30] based on relevant knowledge. Shimu et al. [31] quantified the changes in mangroves from 2011–2019, calculated the normalized vegetation index (NDVI), and quantified vegetation height and area by creating the Floras index. Luo et al. [32] used Landsat TM data to effectively improve the accuracy of mangrove extraction by using a sparse model with multiple features (spectral, topographic, textural, etc.). Zhang et al. [33] applied Worldview-3 and Radarsat-2 to classify mangrove species in the Mai-Po Marshes Nature Reserve using the random forest (RF) method.

A growing number of studies focus on the response of mangroves to global climate change, so there is a need for long-term, continuous observations of mangroves on the national, regional, and global scale. Spalding et al. [17] were the first to assess the distribution of mangroves around the world. Subsequently, large-scale mapping studies of mangroves using low or medium spatial resolution remote sensing data from 2000 onwards, combined with various classification methods, have been carried out [17,34,35]. However, artificially designed features are usually low-level and suitable for objects with sharp edges, shapes, and textures. Traditional classification methods are difficult to apply in practice due to the complexity of scenes in large areas and the spatio-temporal diversity of remote sensing data, so mangrove extraction in large areas remains a challenging problem. This has prompted the development of more powerful and accurate classification schemes.

With the development of computer hardware and the support of big data, deep learning has developed rapidly [36]. Remote sensing mapping of mangroves faces the challenges of limited information extracted from low or medium-resolution images, difficulty in acquiring high-resolution images, and lack of ground survey data for long term [37–39]. Deep learning, represented by convolutional neural networks (CNNs), has been widely used in image recognition [40,41] and information extraction [42,43] because it offers advantages with respect to data processing power and hierarchical learning capabilities. For example, the automatic extraction of feature from remote sensing data by CNNs has greatly improved the classification accuracy of complex features (almost always greater than 90%) [44–47]. CNNs are also applied to other image reconstruction problems, such as image de-noising [48], restoration [49], and texture synthesis [50], by building a library of remote sensing samples and optimizing the model structure. Current available CNNs have greatly improved the ability of models to distinguish between objects through data enhancement [51,52], multi-scale fusion [53], post-processing [54], model reconstruction [55–57], and other optimization methods. Relatively few studies have applied deep learning to mangrove classification, focusing mostly on attempts to classify mangroves in small areas. For example, Faza used deep neural networks to classify mangroves based on their characteristics [58]; Iovan explored mangroves using WorldView2 and Sentinel-2 images based

on deep convolutional neural networks [59]. However, deep learning faces challenges of difficult dataset construction and lack of interpretability in remote sensing applications.

Recently, to address the limitation of CNNs to detect the relationship between features at different locations in an image, Hinton et al. [60] attempted to build an interpretable deep learning model, and proposed the concept of “capsules” as a powerful alternative to CNNs. Each capsule outputs an activation vector rather than a scalar. Further understanding of remote sensing image processing is gained by using the part-whole relationship in images in the context of deep learning. Each capsule learns equivariant representation that is more robust to changes in pose and spatial relationships of parts of objects in images. Considering that mangroves usually grow in the coastal inter-tidal zone and exhibit significant spatial relationship with the surrounding land types, this paper suggests that the advantage of capsule unit extraction of spatial relationships combined with traditional CNNs can help improve the accuracy of mangrove mapping.

Meanwhile, considering the advantage of the compact structure of the U-net, which can train models with limited data [61], this paper develops Capsules-Unet for mangrove extraction from remote sensing images by incorporating “capsules” into the U-net architecture [62]. The network can characterize the remote sensing data at a higher abstraction level to achieve high-precision extraction of mangroves. To address the problem of the huge number of network parameters associated with the original capsule infrastructure, Capsules-Unet significantly reduces the number of these parameters by modifying the original algorithm to improve the efficiency of data processing. This study is the first attempt to apply deep learning methods for large-scale mangrove mapping, expanding the potential of deep learning applications. First, the extraction of Hainan Island mangroves was used to confirm the validity of the model. Then, Capsules-Unet was applied to large-scale mangroves mapping along the MSR from 1990 to 2015, pursuant to fast and accurate extraction of mangrove information. Further, this research provides a scientific basis for the protection, utilization, and ecological restoration of mangroves, by understanding the trends and dynamics of mangroves along the MSR.

## 2. Materials

### 2.1. Study Area

The study area is mainly divided into two parts: the mangrove forest on Hainan Island is used as a small experimental area for the validation of model performance, which facilitates the adjustment of parameters and model structure. On this basis, the Capsules-Unet was extended to large area mapping to obtain the distribution range of mangroves along the MSR.

The Maritime Silk Road starts from China and connects countries and regions along the route from the Western Pacific to the Indian Ocean (as shown in Figure 1). A total of 27 countries, namely China, Vietnam, Cambodia, Thailand, Malaysia, Singapore, Brunei, Philippines, Indonesia, Myanmar, Bangladesh, India, Sri Lanka, Pakistan, Iran, Kuwait, Qatar, United Arab Emirates, Oman, Yemen, Saudi Arabia, Egypt, Sudan, Eritrea, Djibouti, Somalia, and Kenya contain mangroves. The mangroves in these countries span five regions: East Asia, South-East Asia, South Asia, Middle East, and North Africa. The study area is rich in mangrove species and complex in structure, with the highest density of mangrove, and is characterized by complex ecological conditions, frequent land cover conversion, and high incidence of natural disasters such as typhoons and tsunamis.

The study area of Hainan Island was firstly used to verify and evaluate the efficiency and accuracy of the Capsules-Unet model. As shown in Figure 1, Hainan Island, located on the northern edge of the tropics (between  $108^{\circ}37'E$  and  $111^{\circ}03'E$ ,  $18^{\circ}10'N$  and  $20^{\circ}10'N$ ), contains the richest and most widely distributed areas of mangroves in China [25]. It has most of the mangrove species in China, including 26 species of true mangrove plants and 12 species of semi-mangrove plants. At present, the mangroves of Hainan Island are mainly distributed in Dongfang, Xinying Bay, Xinying Harbor, Maniao Harbor, Huachang Bay,

Dongzhai Harbor, and Qinglan Harbor, covering an area of about 4300 m<sup>2</sup> and accounting for 30% of the total area of mangroves in China [63].

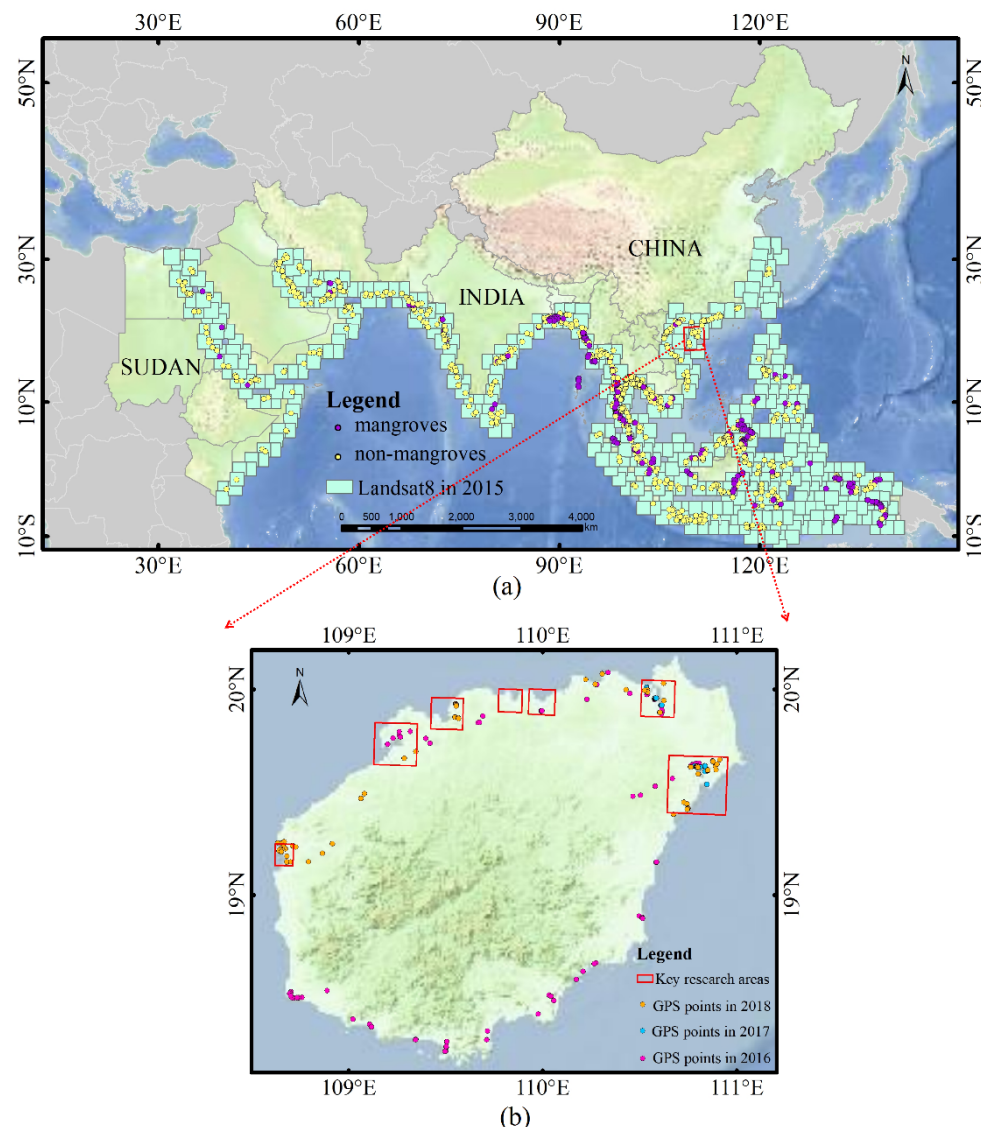


**Figure 1.** Study area. (a) Maritime Silk Road. (b) Hainan Island. (1: Dongfang; 2: Xinying Bay; 3: Xinying Harbor; 4: Maniao Harbor; 5: Huachang Bay; 6: Dongzhai Harbor; 7: Qinglan Harbor).

## 2.2. Landsat Data and Pre-Processing

To extract the extent of mangroves and map their dynamics in the study area over the past few decades, we compared and selected the Landsat data obtained in 1990, 2000, 2010, and 2015. These data were downloaded from the United States Geological Survey in Earth Resources Observation and Science (USGS) (<https://www.usgs.gov/>). Images with less than 20% cloud coverage were selected. However, considering the large study area and the complexity of the landscape, areas with missing images can be collected from adjacent years in order to minimize the data loss due to frequent cloud cover. We collected a total of 708 scenes in 1990 (Landsat5 TM), 747 scenes in 2000 (Landsat5 TM), 607 scenes in 2010 (479 from Landsat5 TM and 128 from Landsat7 ETM+), and 638 scenes in 2015 (Landsat8 OLI). The coverage of Landsat8 in 2015 is shown in Figure 1.

The selected Landsat images were pre-processed by QUAC atmospheric correction, band combination, and image clipping. QUAC atmospheric correction is handled by the relevant ENVI module. As mangroves have very distinct spectral characteristics in the

remote sensing data, especially in the near-infrared band with strong reflectance, they are easier to classify out than other land cover types. In this study, SWIR(short-wave infrared) (1.57–1.67  $\mu\text{m}$ ), NIR(near infrared) (0.85–0.88  $\mu\text{m}$ ), red (0.64–0.67  $\mu\text{m}$ ) bands were used to composite false color images, and mangroves usually appear as dark green in the remote sensing images.

### 2.3. Training and Validation Data for Models

The samples used to train the model were pixel-level, meaning that each pixel in the sample is labeled with an attribute value. Due to the medium resolution of Landsat images, direct visual interpretation is difficult. Therefore, machine learning methods (support vector machine and random forest) were used to initially classify the images, and then GIS tools were used to post-process the misclassification and fragmentation patches in the results through manual discrimination to ensure good internal connectivity, complete boundaries, and correct types of feature categories as much as possible. A total of 1023 patches were obtained to build a more accurate mangrove dataset. About 70% of these samples were derived from 2015 and 30% from 1990–2010. An example of mangrove training samples is shown in Figure 2.

Considering the resolution of the image, patches were firstly cropped to  $64 \times 64$  size using a random sliding window in order to better capture the spatial features of mangroves for the model. The diversity and variability of the data were increased through normalization [64] and data enhancement [65]. Eighty percent of the samples in the dataset were used for training and 20% for validation.

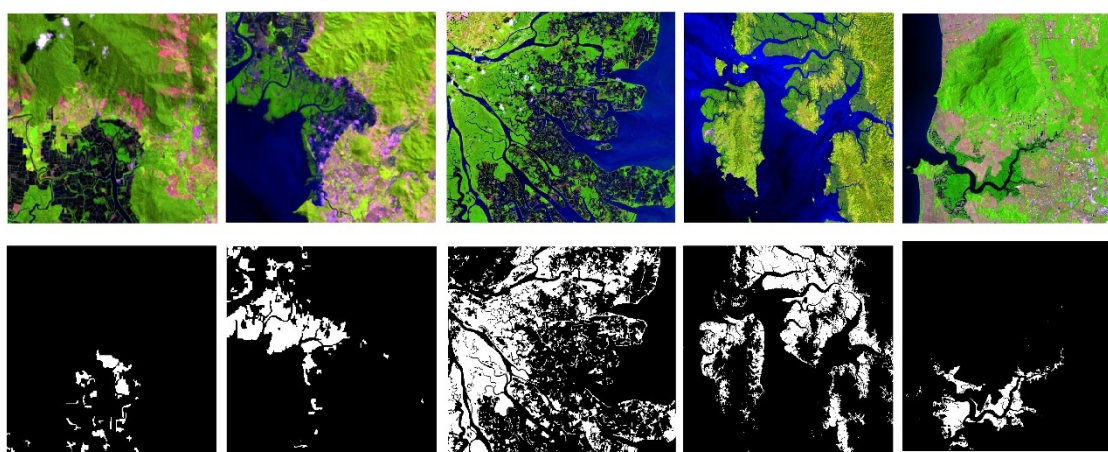


**Figure 2.** Example of training data and validation data. White: mangroves; black: other land types.

### 2.4. Sample of Accuracy Assessment

As the Maritime Silk Road covers a large area, it is not possible to obtain mangrove validation points directly from field surveys. Therefore, we used mangrove datasets which were publicly available online, namely WCMC (Global Distribution of Mangroves USGS (2011)) [17] and GMW (The Global Mangrove Watch) [66], as reference to select mangrove validation samples. Random points were identified using GIS and validation point attributes were determined with reference to high-resolution images of the corresponding years in Google Earth. We deployed 1100, 1103, 1097, and 1101 validation points in 1990, 2000, 2010, and 2015, respectively. Validation points included mangroves and non-mangroves (farm, grass, forests, bare land, water, ponds, artificial surfaces, and salt marshes). The distribution of the validation samples is shown in Figure 1.

In addition, we conducted field surveys of mangroves in Hainan in December 2016, March 2017, and December 2018, and collected a total of 386 validation points. The positional accuracy of GPS points is 2.5 m. A total of 299 sample points located in the seven

study sites were used for mangrove accuracy assessment, comprised of 148 mangrove points and 151 other land use cover points.

### 3. Methods

#### 3.1. U-Net

U-net has an encoder–decoder structure that is widely used in remote sensing image classification due to its high flexibility and superiority [67]. The input image proceeds through the encoder first to generate down-sampled feature maps. The decoder part then implements an up-sampling of the feature mapping to the same size as the original image. U-net is composed of stackable highway units, allowing deeper networks to be trained using a limited number of samples. U-net has been very successful in semantic segmentation on both medical images and RS images by adding skip connections between the encoder and decoder layers with better spatial accuracy.

#### 3.2. Capsules-Unet

The CapsNets network proposed by Hinton theoretically complements the shortcomings of CNNs [60]. Each capsule outputs an activation vector instead of a scalar, which is the biggest difference compared to CNNs. The capsule consists of two parts: the orientation represents certain properties of the object (pose, texture, edge information, etc.), and the length indicates the probability of the category occurring, with a value between 0 and 1. CapsNets uses dynamic routing to update the coupling coefficient, but this required a lot of space to store the relevant parameters which poses difficulties for remote sensing applications.

Considering the advantage of the compact structure of U-net, which can train models with limited data [61], Y. Guo proposed Capsules-Unet for remote sensing classification by incorporating “capsules” into the U-net architecture [62]. Capsule-Unet proposes two improvements on the original dynamic routing algorithm to address the problem of excessive memory burden and large number of parameters. First, child capsules can only be routed to the parent capsule in a defined local window. Second, capsules of the same type in the network share the transformation matrix.

Capsules-Unet and U-net have similar network structures, but use vectors as input and calculation units. Capsules-Unet is composed of four parts: feature extraction module, contracting path module, expansive path module, and classification module. The Capsules-Unet input can be an image of any size; here, it was a  $64 \times 64$  pixel multi-bands image. In this paper, Capsules-Unet was used to extract the spatial distribution of mangroves along the MSR.

#### 3.3. Accuracy Assessment

We used three different indicators for accuracy assessment, namely Kappa coefficient, overall accuracy (OA), and the F1-scores. The Kappa coefficient is a common metric for gauging classification accuracy. OA is a global measure of segmentation accuracy that provides information about the pixel ratio for correct classification. F1-score is an aggregate indicator that reflects the whole, independent of the number of categories; it is the mean of the reconciliation between precision and recall. Precision is defined as the proportion of correctly truth positive samples (TPs) that are actually predicted to be positive, while recall is defined as the ratio of correctly truth positive samples to the proportion of truth positive samples. The above indicators are calculated based on the confusion matrix. In Equation (1), FN is the false negative data, i.e., the number of positive samples incorrectly predicted as negative classes by the classification model:

$$\text{precision} = \frac{\text{TP}}{\text{TP} + \text{FP}}, \text{recall} = \frac{\text{TP}}{\text{TP} + \text{FN}}, \quad (1)$$

$$\text{F1-scores} = \frac{2 \times (\text{precision} \times \text{recall})}{\text{precision} + \text{recall}}. \quad (2)$$

## 4. Results and Discussion

### 4.1. Validation of the Model

The performance of Capsules-Unet was evaluated using mangrove forest located in Hainan Island as an example. The experiments were carried out in terms of both classification accuracy and computational efficiency, and were compared with U-net in the same experimental setting.

Compared to U-net, Capsules-Unet identifies the mangroves almost completely (Figure 3). In addition, Capsules-Unet can effectively avoid the effects of image noise through multi-layer convolution operation, so that it can provide clear boundaries and good area connectivity for mangrove discrimination. U-net also obtained good classification results, however, there were many misclassified pixels in small areas near the mangrove boundaries. This experiment showed that U-net had more difficulty in processing detailed information and tiny features in images. As mangroves are usually located in the intertidal zone between land and sea, they have a clear spatial relationship with surrounding objects, and Capsules-Unet learns not only the features themselves, but also the part-whole relationships between features through the capsule form.

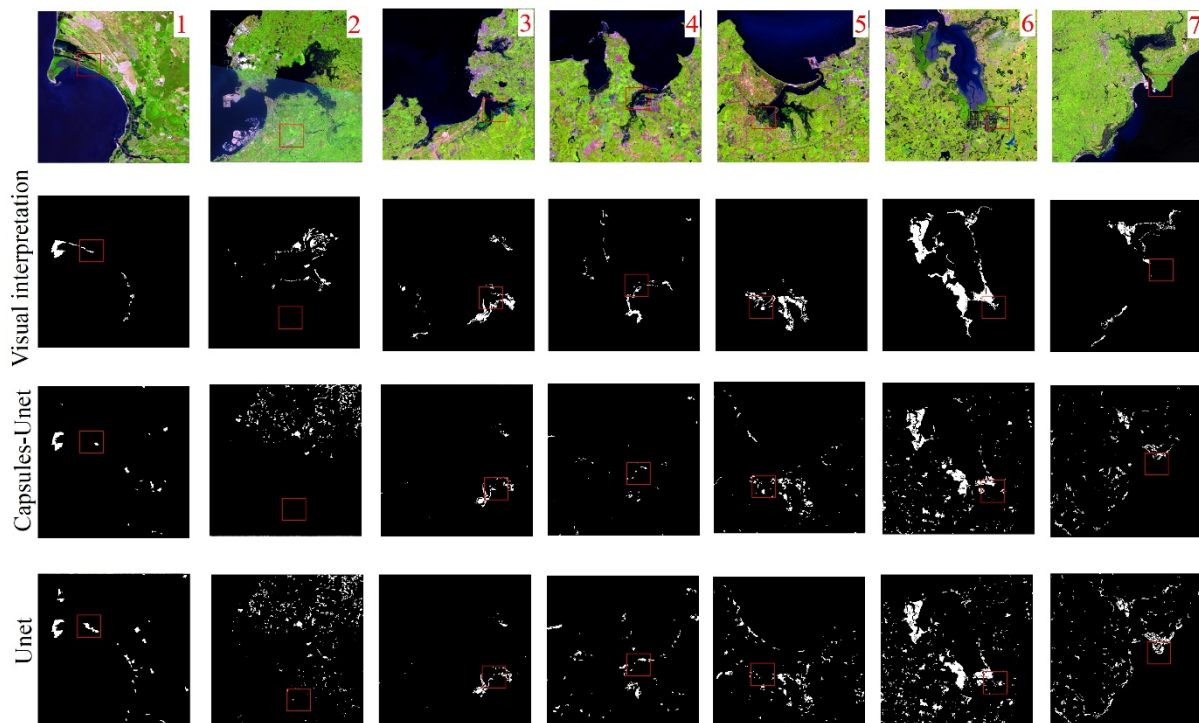


**Figure 3.** Results of the classification of mangrove sites in Hainan Island. 1: Dongfang; 2: Xinying Bay; 3: Xinying Harbor; 4: Maniao Harbor; 5: Huachang Bay; 6: Dongzhai Harbor; 7: Qinglan Harbor. White: mangroves; black: other land types. The red square is to facilitate highlighting the different results of the two methods.

From Table 1, the OA, Kappa coefficient, and F1-scores for Capsules-Unet are 86%, 0.73, and 0.86 respectively, higher than U-net, indicating the superior classification accuracy of the proposed method.

We also evaluated the computational efficiency of Capsules-Unet and U-net by the number of network parameters, training time, and FLOPS(floating-point operations per second) (Table 2) under the same computing environment and input parameters. The results showed that the U-net model has more parameters than Capsules-Unet. In the same dataset, Capsules-Unet has only about 5.6 M parameters, which is 81.4% less than U-net (30.1 M). In networks with similar network depths, fewer model parameters allow for a more compact model. However, for the same number of training sessions, the

execution time of Capsules-Unet is 25% longer than the U-net model. The training time is influenced by several factors such as memory storage, computational environment, and neural network contingency. FLOPS, used to evaluate computational efficiency and model complexity, also reflects this, with values of about 2.1 G for Capsules-Unet and 0.87 G for U-net. Since Capsules-Unet and U-net have similar network structure, the higher computational costs of Capsules-Unet are the result of capsules.

**Table 1.** Accuracy assessment for Capsules-Unet and U-net classification results.

Capsules-Unet						U-Net							
OA (%)	Kappa	F1	Mangroves (%)		Non-Mangroves (%)		OA (%)	Kappa	F1	Mangroves (%)		Non-Mangroves (%)	
			1	2	1	2				1	2	1	2
			UA	PA	UA	PA				UA	PA	UA	PA
86	0.73	0.86	83	90	89	82	81	0.62	0.79	74	85	84	77

<sup>1</sup> UA is user's accuracy, <sup>2</sup> PA is producer's accuracy.

**Table 2.** Model parameters for Capsules-Unet and U-net.

	Number of Layers	Number of Parameter	Running Time	FLOPS
Capsules-Unet	13	~5.6 M	~48 h	~2.1 G
U-net	19	~30.1 M	~38 h	~0.87 G

Accuracy–loss curves of Capsules-Unet and U-net are shown in Figure 4. The accuracy curve is used to measure the performance of the model, while the loss curve is used to further optimize the model. Figure 4 shows that Capsules-Unet has higher accuracy and lower loss. Therefore, Capsules-Unet converges faster than U-net and can achieve almost optimal performance in a short period of time.

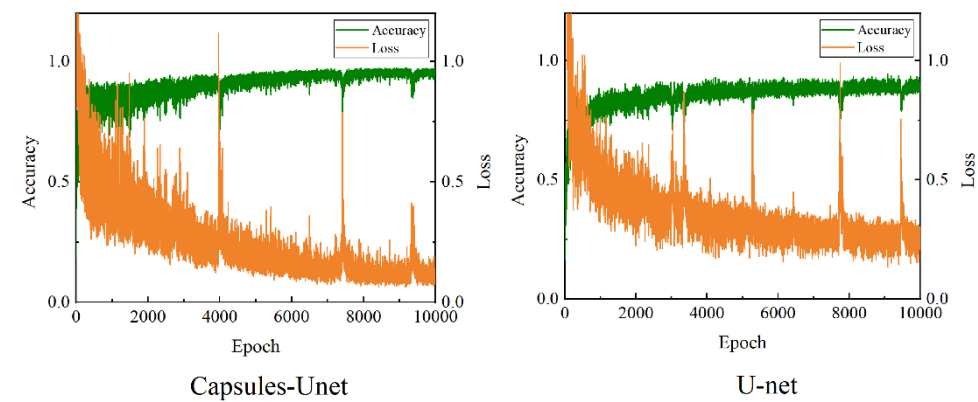


**Figure 4.** Accuracy–loss curves for Capsules-Unet and U-net.

In sum, by the above comparison, it can be concluded that Capsules-Unet can achieve better classification results with a lower computational cost.

#### 4.2. Classification Results of the Maritime Silk Road

Based on the validation of the effectiveness of the Capsules-Unet model, we applied the trained model to large area mapping. Landsat images obtained in 1990, 2000, 2010, and 2015 were analyzed and compared to monitor the extent and dynamics of mangroves along the MSR over decades (Figure 5). From Figure 5, it can be seen that mangroves are distributed in Ref [27] countries along the route, with the most intensive distribution in

Southeast Asia. Mangroves are relatively less common in North Africa due to differences in topography, climate, and ocean circulation.

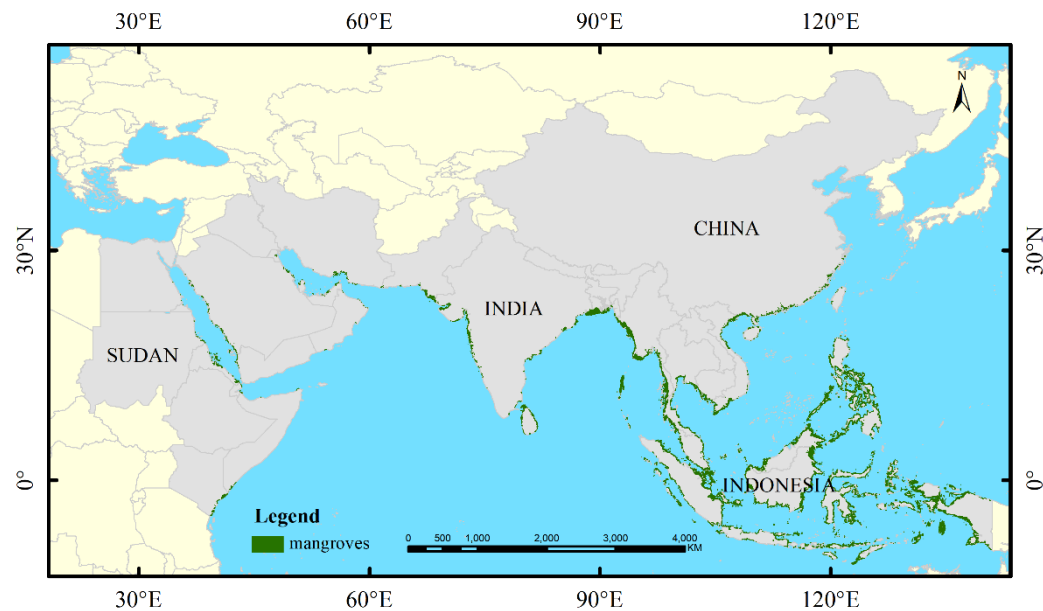


**Figure 5.** The distribution of mangroves along the Maritime Silk Road in 2015.

Figure 6 shows the mangrove extraction results from four period images in five different regions. Although the geographic and climatic conditions are quite different in the five regions, better mangroves extraction results are still obtained. Since the majority of the model's training samples are from 2015, the results for that year have better classification and less confounding with other features compared to other years. Geographic location also affects the accuracy of mangrove classification, and the ecological characteristics of mangrove systems can vary significantly from region to region due to differences in water and soil salinity, ocean circulation, tides, topography, soils, climate, and biological factors. For example, the mangroves in area Figure 6a and area Figure 6b are located in shallows with a dense distribution of surrounding vegetation types, so there are varying degrees of mixing of mangroves with other vegetation in the images of the four phases. The mangroves in area Figure 6c are located in an estuarine delta, which is one of the most frequent areas of land type conversion. The mangroves are narrow and fragmented, which makes extraction difficult. Mangroves in area Figure 6d are located in North Africa, where the surrounding land types are mainly bare desert beaches with distinct mangrove features, so the extracted mangroves are well-defined and complete in size. Area Figure 6e is located in Kenya, which is perennially affected by cloud cover and the image quality obtained here is poor. Although the influence of cloud cover was taken into account in the selection of images in this study, it is not possible to mitigate this issue entirely.

As shown in Table 3, the overall accuracy of mangrove classification in 1990, 2000, 2010, and 2015 was 86.9%, 87.3%, 85.7%, and 88.7%, respectively. The Kappa coefficients were 0.64, 0.66, 0.61, and 0.71, respectively. The generally higher extraction accuracy of mangroves in 2015 is related to the number of model training samples and the fact that images and training samples have similar data distributions. F1-scores are a comprehensive measure of classification accuracy. F1-scores were 0.72, 0.74, 0.69, and 0.78 in 1990, 2000, 2010, and 2015, respectively. The classification accuracy of the four period images meets the requirements of the experimental study, demonstrating that Capsules-Unet could successfully be applied to other case-study contexts.

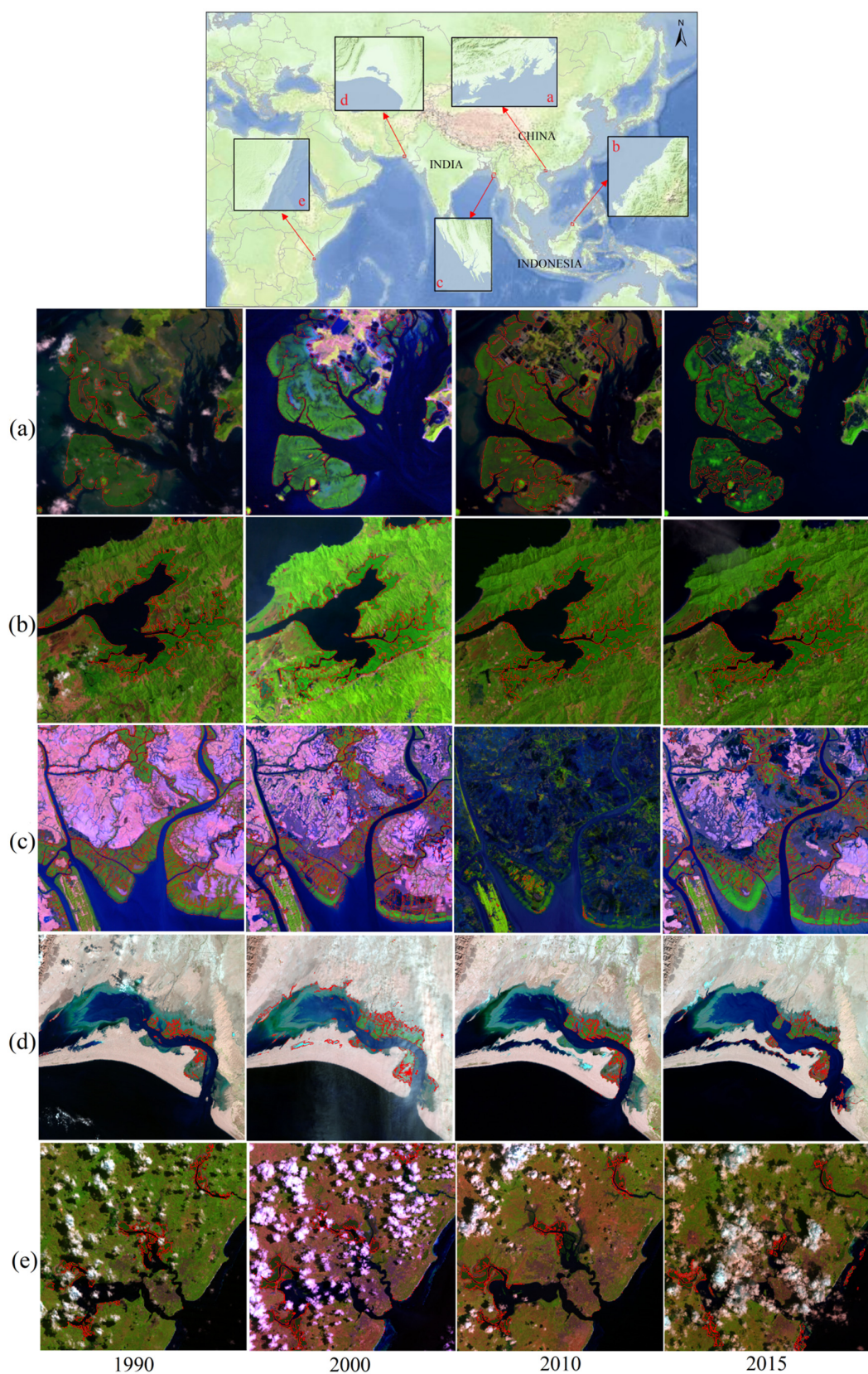


**Figure 6.** Comparison of mangrove extraction in different areas from 1990 to 2015. The red line is the boundary of the mangrove. (a,b) the mangroves are located in shallows; (c) the mangroves are located in an estuarine delta; (d) the mangroves are located in North Africa; (e) the mangroves are located in Kenya.

**Table 3.** Accuracy assessment of mangrove classification results from 1990 to 2015.

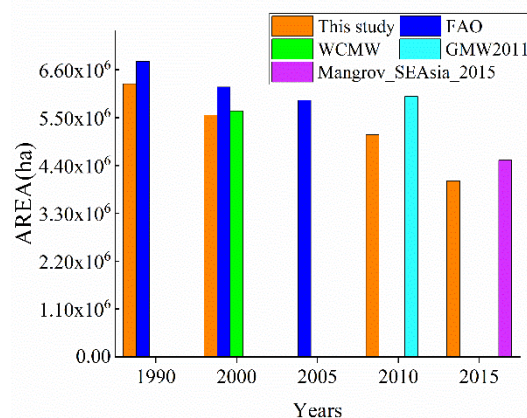
	Mangroves (%)		Non-Mangroves (%)		OA (%)	Kappa	F1
	<sup>1</sup> UA	<sup>2</sup> PA	<sup>1</sup> UA	<sup>2</sup> PA			
1990	90.1	60.8	86.1	97.3	86.9	0.64	0.72
2000	89.6	63.3	86.8	97.0	87.3	0.66	0.74
2010	89.6	56.1	84.9	97.4	85.7	0.61	0.69
2015	86.3	71.3	89.4	95.5	88.7	0.71	0.78

<sup>1</sup> UA is user's accuracy, <sup>2</sup> PA is producer's accuracy.

Moreover, this study can ensure the consistency of spatially referenced multi-temporal data analysis, improve extraction accuracy, and enhance the spatial variation logic of mangroves by using continuous and consistent remote sensing images and a classification algorithm with good generalization capability.

#### 4.3. Comparison and Analysis with Other Data Sets

Current estimates of the total global mangrove area range from 11,000,000 to 24,000,000 ha [2,68]. In this study, we firstly compared the statistical results obtained by Capsules-Unet with publicly available data from FAO (The Food and Agriculture Organization) [69], WCMC (Global Distribution of Mangroves USGS (2011)) [17], GMW2011 (The Global Mangrove Watch) [66], and Mangrove\_SEAsia\_2015 [70] (Appendix A and Figure 7). These publicly available datasets have the same statistical regions as this study and are compared. The FAO estimates are compiled from different data and do not provide sufficiently detailed spatial information. The WCMC dataset was produced by interpreting approximately 1000 Landsat images using supervised and unsupervised image classification techniques with reference to Global Land Survey (GLS) data. The GMW2011 was completed and the global mangrove distribution map in 2000 was obtained by using ALOS PALSAR (radar) and Landsat (optical) data. The Mangrove\_SEAsia\_2015 data were extracted for mangroves in Southeast Asia using 428 Landsat-8 images from 2013 to 2015, ASTER GDEM data, and a multi-classifier combination approach.

**Figure 7.** Comparison of mangroves area from different data sets.

The statistics in 1990 from this study are generally consistent with the FAO. The results in 2010 and 2015 differ from the GMW2011 and Mangrove\_SEAsia\_2015. Factors such as the spatial resolution of the remote sensing images, tidal inundation, and information extraction strategy can affect the accuracy of mangrove extraction. Related studies have shown that the area error of remote sensing image measurements will gradually increase as the spatial resolution increases [71]. Therefore, for narrow-belt, fragmented mangrove areas, low and medium resolution remote sensing images are not effective for extraction. In addition, tides usually inundate areas of mangrove forests, especially the sparse and

low-growing forest. When using optical remote sensing technology to extract information on the distribution of mangroves, it is difficult to detect submerged mangroves due to the absorption of electromagnetic waves by water (Figure 8). The most effective way to ensure that spatial information concerning submerged mangroves is extracted accurately is to obtain remote sensing images of exposed beaches or to use radar images [72]. In fact, due to the specific spatial distribution of mangroves and the simplicity of adjacent vegetation types, generally, a machine learning method can extract mangrove spatial distribution information with an accuracy close to or exceeding 95% using high-resolution ( $<2.5$  m) optical images of dense mangroves and exposed beaches [73,74]. For national or regional scales, the technical challenges for accurate monitoring of the spatial distribution of mangroves is the extraction of sparse, low-growing young forests and narrow mangrove belts along embankments.

Currently available datasets ensure that the spatial distribution of mangroves is extracted as reliably as possible through the selection of appropriate remote sensing images, classification methods, and the necessary post-processing processes. Compared with previous research, this study developed and used a generalizable classification technique and consistent data sources to better map mangroves, which is useful for continuous spatial change monitoring and evolution analysis of mangroves.

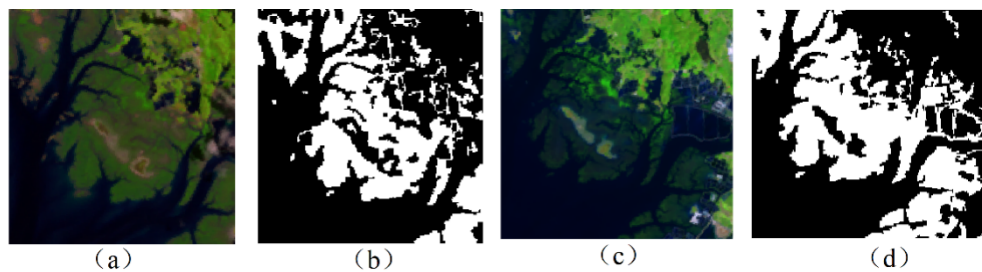


**Figure 8.** Tidal inundation of mangroves, (a) non-inundation. The data was obtained on 5 July 2010. (b) Classification results of non-inundation using Capsules-Unet, (c) inundation. The data was obtained on 25 October 2010. (d) Classification results of inundation using Capsules-Unet. White: mangroves; black: other land types.

#### 4.4. The Distribution and Dynamics of Mangrove Areas

Before determining mangrove areas, this study manually deleted noise from the classification results and corrected the attributes of erroneous categories to avoid affecting the statistical results.

The statistical results of this study show an overall decreasing trend in the area of mangroves along the MSR from 1990 to 2015. From Figure 9, it can be seen that 1,356,686 ha (about 21.5%) of the mangrove in the study area disappeared during the 25 years from 1990 to 2015. The area of mangrove decreased by 751,446 ha, 446,925 ha, and 15,835 ha between 1990 and 2000, 2000 and 2010, and 2010 and 2015, respectively, and the average annual rate of change of mangrove area continued to decrease by  $-1.19\%$ ,  $-0.80\%$ , and  $-0.62\%$ , respectively.

From Figure 10 and Appendix A, it can be observed that the area of mangrove wetlands in Southeast Asia continued to shrink and the rate of decline accelerated from 1990 to 2015. In 1990, 2000, 2010, and 2015, the area of mangrove wetlands was 5,279,677 ha, 4,552,205 ha, 4,047,106 ha, and 3,846,226 ha, respectively, with an average annual rate of change of  $-1.37\%$ ,  $-1.10\%$ , and  $-0.99\%$ . Mangrove losses were particularly high in Indonesia, Vietnam, Thailand, and Myanmar. The continued decline of mangroves is mainly due to agricultural (Figure 10b), aquaculture, tourism, urban development, and overdevelopment [75]. For example, in some countries such as Thailand and Myanmar, shrimp pond farming and rice cultivation are the main drivers of mangrove changes [76,77]. Related studies likewise show that a total of  $424.26 \text{ km}^2$  of mangroves were destroyed in Thailand between 1985 and 2015, of which  $376.39 \text{ km}^2$  were reclaimed for aquaculture [78].

Mangrove forests in areas close to land are rapidly decreasing due to polder farming; they are expanding seaward on tidal flats (Figure 10a). In Indonesia, the loss of mangroves is mainly attributed to palm oil plantations [79]. In addition, mangrove wetlands in this region are located in areas of high seismic activity and are vulnerable to tsunamis, hurricanes, and other natural phenomena [80,81]. Mangroves area in China for the period around 2015 from our study is consistent with that from a previous study (19,144 versus 19,220 ha) [82]. China's mangroves disappear at a slower rate due to increased conservation awareness.

The mangrove area in South Asia declined by 25,471 ha between 1990 and 2000, with an average annual rate of change of  $-0.27\%$ , as shown in Figure 10 and Appendix A. The loss of mangroves was mainly attributed to human activities such as land cover conversion [34], pollution [83], over-harvesting for timber [84], and natural phenomena including cyclones, tsunamis, and coastal erosion [85]. Over the next 15 years, the area of mangroves continuously increased to 1,016,010 ha by 2015. The mangrove area in India has grown significantly, increasing by about 19.2% over 25 years (Kambo research results are in agreement with us, the mangrove cover has shown an increase of 21.6%) [86]. The Sundarbans, located mainly at the India-Bangladesh border, is the largest mangrove ecosystem in the world, where environmental protection is valued and ecological conditions continue to improve [87].

Mangroves are uncommon in the Middle East and, where they do occur, it is usually in small estuaries. Most mangrove forests are located in Iran (mainly in the Gulf of Oman) and Saudi Arabia (mainly on the Red Sea and Gulf of Aden coasts). From Figure 10 and Appendix A, it can be discerned that the area of mangroves increased from 24,520 to 24,695 ha between 1990 and 2000, with an average annual growth rate of  $0.07\%$ . By 2015, the mangrove area decreased to 21,603 ha. Related studies indicate that mangroves in the Middle East may be at significant risk from climate change due to reduced precipitation, high evaporation rates, increased salinity, and temperatures exceeding maximum tolerances [88–90].

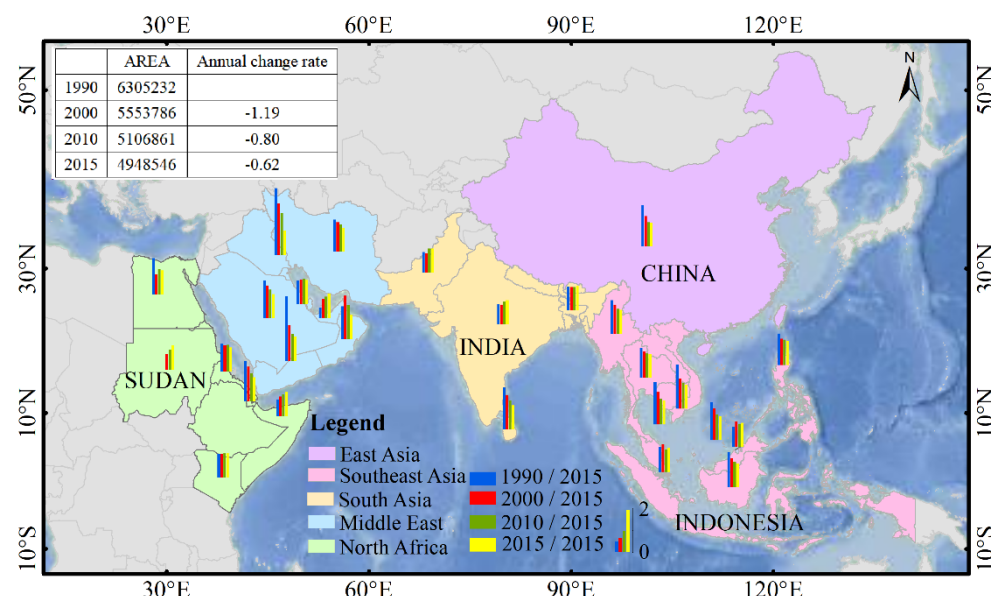


**Figure 9.** The changes in mangrove area in different countries from 1990 to 2015.

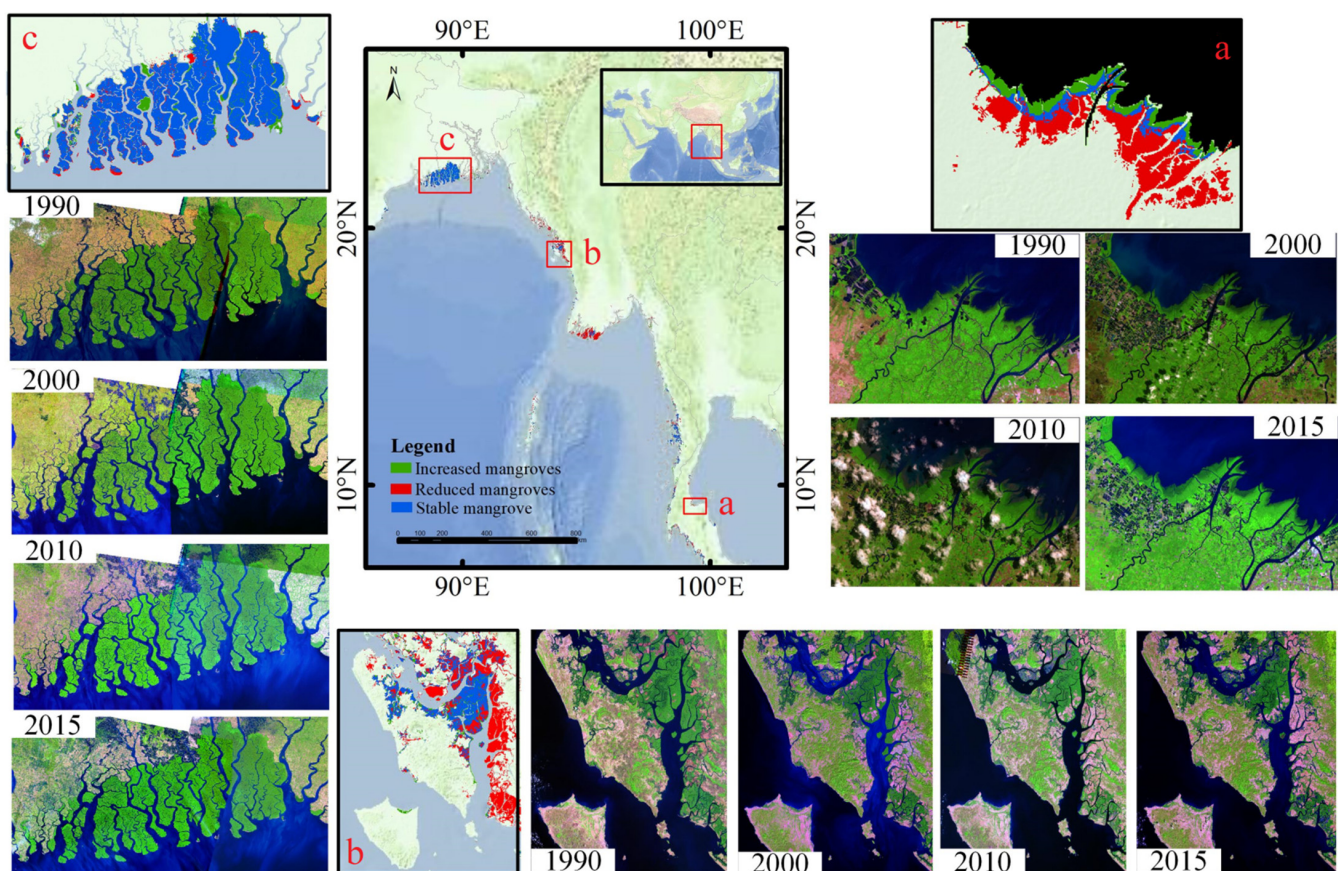


**Figure 10.** Monitoring of mangrove changes along the Maritime Silk Road from 1990 to 2015. ((a): Western Gulf of Thailand; (b): East Bay of Bengal; (c): Sundarbans).

In 2001, Africa accounted for more than 20% of the world's mangrove area [17]. This study focuses on the North African region, which is located on the MSR. Mangroves in this region are scattered along the coast in various deltas, estuaries, and atolls, influenced by temperature and ocean circulation [91]. The area of mangroves increased from 62,256 ha in 1990 to 64,707 ha in 2015, as shown in Appendix A. The average annual rate of change was 0.21%, 0.14%, and 0.05% in 1990–2000, 2000–2010, and 2010–2015, respectively. The figure shows that the area of mangroves in the Sudan, Somalia, and Kenya has continued to increase over the past 25 years.

Mangroves along the MSR exhibit remarkable differences in species diversity. The ecological complexity of the region, where mangroves are being affected by rapid and large-scale agricultural and aquaculture activities, poses significant policy challenges for mangrove conservation and management [92], which may be exacerbated by future climate change impacts.

## 5. Conclusions

In this study, we constructed a mangrove sample dataset and developed the Capsules-Unet model for mapping the distribution and dynamics of mangroves along the MSR from 1990 to 2015. The results showed that there were 4,948,546 ha of mangroves along the Maritime Silk Road in 2015. The overall mapping accuracy of mangroves in 1990, 2000, 2010, and 2015 was 86.9%, 87.3%, 85.7%, and 88.7%, respectively. The average annual rate of change of mangroves was  $-0.96\%$  between 1990 and 2015, with 1,356,686 ha (about 21.5%) of mangroves in the study area lost during this period. Anthropic activities such as agriculture, aquaculture, tourism, urban development, and over-development appear to be the likely drivers of this continued decline. Southeast Asia has experienced the highest

mangrove losses, but the decline has slowed in recent years. Mangroves in South Asia are slowly increasing by virtue of conservation policies. Geo-spatial analysis spanning long time series provides effective support for a better understanding of mangroves dynamics in the study area; this can be leveraged by governmental decision-makers to optimize policy interventions pursuant of the long-term conservation and sustainability of mangroves. This study is a useful attempt to address the remote sensing applications using deep learning algorithms. In the future, in order to improve the accuracy of large-scale mangrove mapping and better understand the evolution process of mangroves, a large and accurate database of mangrove samples should be constructed, and the change process of mangroves over time should be emphasized when designing deep learning models.

**Author Contributions:** Y.G. and J.L. proposed and designed the technique roadmap. Y.G. contributed to the algorithmic methods. Y.G. and G.S. collected the image data. J.L. and G.S. helped with analysis and reviewed the manuscript. All authors have read and agreed to the published version of the manuscript.

**Funding:** This work was funded by the Strategic Priority Research Program of the Chinese Academy of Sciences (Grant No. XDA19030302) and Hainan Provincial Department of Science and Technology (Grant No. ZDKJ2019006).

**Data Availability Statement:** The data are not publicly available due to the confidentiality of the research projects.

**Acknowledgments:** The authors are grateful to those colleagues who assisted with the field surveys and data collection, and would like to express thanks to the anonymous reviewers for their voluntary work and the constructive comments to improve this manuscript.

**Conflicts of Interest:** The authors declare no conflict of interest.

## Appendix A

**Table A1.** Statistical results and comparison of mangroves in different data sets.

Country/Area	1990 (ha)		2000 (ha)		2005 (ha)		2010 (ha)		2015 (ha)		Average Annual Rate of Change in This Study			
	FAO	This Study	FAO	WCMC	This Study	FAO	GMW2011	This Study	Mangrove_SEAsia_2015	This Study	1990–2000	2000–2010	2010–2015	
East Asia	China	38,344	32,871	22,955	17,925	2180	22,480	17,179	19,325	14,397	19,144	-2.64	-2.00	-0.18
	Vietnam	213,500	200,038	157,500	215,529	135,837	157,500	158,218	116,672	120,693	109,590	-3.20	-1.41	-1.21
	Cambodia	82,400	67,713	73,600	47,572	52,080	69,200	59,141	41,850	52,929	38,430	-2.30	-1.96	-1.63
	Thailand	250,200	275,749	244,100	245,120	246,080	240,000	224,464	225,390	412,570	223,630	-1.07	-0.84	-0.15
South-East Asia	Malaysia	642,000	372,908	589,500	558,580	463,216	565,000	530,654	422,260	705,237	443,698	2.42	-0.88	1.01
	Singapore	500	613	500	582	682	500	599	550	263	591	1.12	-1.93	1.49
	Brunei	-	25,296	-	11,089	21,300	-	15,075	17,184	17,032	15,983	-1.57	-1.93	-1.39
	Philippines	273,000	344,338	250,000	259,037	285,950	240,000	289,042	277,973	112,681	262,094	-1.69	-0.27	-1.14
South Asia	Indonesia	3,500,000	3,293,611	3,150,000	2,707,623	2,744,310	2,900,000	3,183,529	2,434,750	2,580,486	2,256,321	-1.66	-1.12	-1.46
	Myanmar	536,100	666,540	516,700	507,579	578,570	507,000	509,226	491,152	508,515	476,745	-1.31	-0.51	-0.58
	Bangladesh	460,000	510,008	476,000	445,679	506,133	476,000	440,257	500,970	-	520,850	-0.07	-0.10	0.79
	India	467,000	321,610	448,200	486,846	309,450	448,000	380,062	356,583	-	383,566	-0.37	1.52	1.51
Middle East	Sri Lanka	9300	24,714	9000	21,564	20,320	8800	23,805	17,010	-	14,330	-1.77	-1.62	-3.15
	Pakistan	207,000	82,447	158,000	50,748	77,405	157,000	64,327	97,543	-	97,264	-0.61	2.60	-0.05
	Iranian	22,500	6817	19,100	12,099	6260	19,000	7868	5772	-	5124	-0.81	-0.78	-2.23
	Kuwait	-	526	-	0	404	5	0	330	-	189	-2.31	-1.83	-8.54
North Africa	Saudi Arabia	20,000	12,547	20,000	8117	10,885	20,000	7501	9400	-	7973	-1.32	-1.36	-3.03
	Qatar	500	610	500	407.3	624	500	442	644	-	616	0.22	0.32	-0.86
	United Arab Emirates	3800	3020	4000	11,071	5663	4100	7654	6321	-	7185	8.74	1.16	2.72
	Oman	2000	395	1000	265	523	1000	162	409	-	291	3.24	-2.17	-5.77
North Africa	Yemen	950	605	900	1071	336	900	1313	253	-	225	-4.44	-2.47	-2.21
	Egypt	500	89	500	34	49	500	202	61	-	59	-4.49	2.44	-0.65
	Sudan	500	0	500	280	442	500	356	559	-	668	-	2.64	3.89
	Eritrea	6500	6926	6400	4969	6585	6400	7526	6683	-	6051	-0.49	0.14	-1.89
Kenya	Djibouti	1000	663	1000	551	570	1000	520	457	-	395	-1.40	-1.98	-2.71
	Somali	8600	4479	7800	2134	5300	7300	2472	5874	-	6512	1.83	1.08	2.27
	Kenya	52,000	50,099	50,000	39,948	50,632	50,000	58,059	50,886	-	51,022	0.01	0.05	0.05

## References

1. Thomas, N. The Global Mangrove Watch (GMW): Mapping global mangrove baseline and time-series changes in extent with ALOS PALSAR. In Proceedings of the IGARSS 2015—2015 IEEE International Geoscience and Remote Sensing Symposium, Milan, Italy, 26–31 July 2015.
2. Shahbudin, S.; Zuhairi, A.; Kamaruzzaman, B.Y. Impact of coastal development on mangrove cover in Kilim river, Langkawi Island, Malaysia. *J. For. Res.* **2012**, *23*, 185–190. [[CrossRef](#)]
3. Tang, W.; Zheng, M.; Zhao, X.; Shi, J.; Yang, J.; Trettin, C. Big Geospatial Data Analytics for Global Mangrove Biomass and Carbon Estimation. *Sustainability* **2018**, *10*, 472. [[CrossRef](#)]
4. Barua, P.; Rahman, S. Sustainable Livelihood of Vulnerable Communities in Southern Coast of Bangladesh through the Utilization of Mangroves. *Asian J. Water Environ. Pollut.* **2019**, *16*, 59–67. [[CrossRef](#)]
5. Chandra, G. Observation and Monitoring of Mangrove Forests Using Remote Sensing: Opportunities and Challenges. *Remote Sens.* **2016**, *8*, 783.
6. Makowski, C.; Finkl, C.W. Erratum to: Threats to Mangrove Forests: Hazards, Vulnerability, and Management. In *Threats to Mangrove Forests*; Springer: Berlin, Germany, 2018.
7. Wang, L.; Jia, M.; Yin, D.; Tian, J. A review of remote sensing for mangrove forests: 1956–2018. *Remote Sens. Environ.* **2019**, *231*, 111223. [[CrossRef](#)]
8. Carugati, L.; Gatto, B.; Rastelli, E.; Lo Martire, M.; Coral, C.; Greco, S.; Danovaro, R. Impact of mangrove forests degradation on biodiversity and ecosystem functioning. *Sci. Rep.* **2018**, *8*, 13298. [[CrossRef](#)]
9. Spalding, M. *World Atlas of Mangroves*; Routledge: New York, NY, USA, 2010.
10. Yao-Dong, D.U.; Xu-Hua, C.; Xian-Wei, W.; Hui, A.; Hai-Lai, D.; Jian, H.; Xiao-Xuan, W. A Review of Assessment and Adaptation Strategy to Climate Change Impacts on the Coastal Areas in South China. *Adv. Clim. Chang. Res.* **2013**, *4*, 201–207. [[CrossRef](#)]
11. Rivera-Monroy, V.H.; Danielson, T.M.; Castañeda-Moya, E.; Marx, B.D.; Travieso, R.; Zhao, X.; Farfan, L.M. Long-term demography and stem productivity of Everglades mangrove forests (Florida, USA): Resistance to hurricane disturbance. *For. Ecol. Manag.* **2019**, *440*, 79–91. [[CrossRef](#)]
12. Simard, M.; Fatoyinbo, L.; Smetanka, C.; Rivera-Monroy, V.H.; Castañeda-Moya, E.; Thomas, N.; Vander Stocken, T. Mangrove canopy height globally related to precipitation, temperature and cyclone frequency. *Nat. Geosci.* **2019**, *12*, 40–45. [[CrossRef](#)]
13. Pranchai, A.; Jenke, M.; Berger, U. Well-intentioned, but poorly implemented: Debris from coastal bamboo fences triggered mangrove decline in Thailand. *Mar. Pollut. Bull.* **2019**, *146*, 900–907. [[CrossRef](#)]
14. Gandhi, S.; Jones, T. Identifying Mangrove Deforestation Hotspots in South Asia, Southeast Asia and Asia-Pacific. *Remote Sens.* **2019**, *11*, 728. [[CrossRef](#)]
15. Thant, Y.M.; Kanzaki, M.; Ohta, S.; Than, M.M. Carbon sequestration by mangrove plantations and a natural regeneration stand in the Ayeyarwady Delta, Myanmar. *Tropics* **2012**, *21*, 1–10. [[CrossRef](#)]
16. Bryan-Brown, D.N.; Connolly, R.M.; Richards, D.R.; Adame, F.; Friess, D.A.; Brown, C.J. Global trends in mangrove forest fragmentation. *Sci. Rep.* **2020**, *10*, 7117. [[CrossRef](#)]
17. Giri, C.; Ochieng, E.; Tieszen, L.L.; Zhu, Z.; Singh, A.; Loveland, T.; Masek, J.; Duke, N. Status and distribution of mangrove forests of the world using earth observation satellite data: Status and distributions of global mangroves. *Glob. Ecol. Biogeogr.* **2011**, *20*, 154–159. [[CrossRef](#)]
18. Sreelekshmi, S.; Nandan, S.B.; Sreejith, V.K.; Radhakrishnan, C.K.; Suresh, V.R. Mangrove species diversity, stand structure and zonation pattern in relation to environmental factors—A case study at Sundarban delta, east coast of India. *Reg. Stud.* **2020**, *35*, 101111. [[CrossRef](#)]
19. Thomas, N.; Lucas, R.; Bunting, P.; Hardy, A.; Rosenqvist, A.; Simard, M. Distribution and drivers of global mangrove forest change, 1996–2010. *PLoS ONE* **2017**, *12*, e0179302. [[CrossRef](#)] [[PubMed](#)]
20. Bhattacharai, B. Assessment of mangrove forests in the Pacific region using Landsat imagery. *J. Appl. Remote Sens.* **2011**, *5*, 3509. [[CrossRef](#)]
21. Worthington, T.A.; Ermgassen, P.S.E.Z.; Friess, D.A. A global biophysical typology of mangroves and its relevance for ecosystem structure and deforestation. *Sci. Rep.* **2020**, *10*, 14652. [[CrossRef](#)]
22. Mondal, P.; Liu, X.; Fatoyinbo, T.E.; Lagomasino, D. Evaluating Combinations of Sentinel-2 Data and Machine-Learning Algorithms for Mangrove Mapping in West Africa. *Remote Sens.* **2019**, *11*, 2928. [[CrossRef](#)]
23. Yancho, J.M.M.; Jones, T.G.; Gandhi, S.R.; Ferster, C.; Lin, A.; Glass, L. The Google Earth Engine Mangrove Mapping Methodology (GEEMMM). *Remote Sens.* **2020**, *12*, 3758. [[CrossRef](#)]
24. Cavanaugh, K.C.; Osland, M.J.; Bardou, R.; Hinojosa-Arango, G.; López-Vivas, J.M.; Parker, J.D.; Rovai, A.S. Sensitivity of mangrove range limits to climate variability. *Glob. Ecol. Biogeogr.* **2018**, *27*, 925–935. [[CrossRef](#)]
25. Liao, J.; Zhen, J.; Zhang, L.; Metternicht, G. Understanding Dynamics of Mangrove Forest on Protected Areas of Hainan Island, China: 30 Years of Evidence from Remote Sensing. *Sustainability* **2019**, *11*, 5356. [[CrossRef](#)]
26. Gupta, K.; Mukhopadhyay, A.; Giri, S.; Chanda, A.; Majumdar, S.D.; Samanta, S.; Hazra, S. An Index for discrimination of mangroves from non-mangroves using LANDSAT 8 OLI imagery. *MethodsX* **2018**, *5*, 1129–1139. [[CrossRef](#)] [[PubMed](#)]

27. Kamal, M.; Phinn, S.; Johansen, K.; Adi, N.S. Estimation of mangrove leaf area index from ALOS AVNIR-2 data (A comparison of tropical and sub-tropical mangroves). In Proceedings of the Advances of Science and Technology for Society: Proceedings of the 1st International Conference on Science and Technology 2015 (ICST-2015), Yogyakarta, Indonesia, 11–13 July 2016.
28. Alam, S.M.R.; Hossain, M.S. A Rule-Based Classification Method for Mapping Saltmarsh Land-Cover in South-Eastern Bangladesh from Landsat-8 OLI. *Can. J. Remote Sens.* **2020**, *1*–25. [[CrossRef](#)]
29. Heumann, B.W. An Object-Based Classification of Mangroves Using a Hybrid Decision Tree—Support Vector Machine Approach. *Remote Sens.* **2011**, *3*, 2440–2460. [[CrossRef](#)]
30. Wang, T.; Zhang, H.; Lin, H.; Fang, C. Textural-Spectral Feature-Based Species Classification of Mangroves in Mai Po Nature Reserve from Worldview-3 Imagery. *Remote Sens.* **2015**, *8*, 24. [[CrossRef](#)]
31. Shimu, S.A.; Aktar, M.; Afjal, M.I.; Nitu, A.M.; Uddin, M.P.; Al Mamun, M. NDVI Based Change Detection in Sundarban Mangrove Forest Using Remote Sensing Data. In Proceedings of the 2019 4th International Conference on Electrical Information and Communication Technology (EICT), Khulna, Bangladesh, 20–22 December 2019.
32. Luo, Y.M.; Ouyang, Y.; Zhang, R.C.; Feng, H.M. Multi-Feature Joint Sparse Model for the Classification of Mangrove Remote Sensing Images. *ISPRS Int. J. Geo-Inf.* **2017**, *6*, 177. [[CrossRef](#)]
33. Zhang, H.; Wang, T.; Liu, M.; Jia, M.; Lin, H.; Chu, L.M.; Devlin, A.T. Potential of Combining Optical and Dual Polarimetric SAR Data for Improving Mangrove Species Discrimination Using Rotation Forest. *Remote Sens.* **2018**, *10*, 467. [[CrossRef](#)]
34. Giri, C.; Long, J.; Abbas, S.; Murali, R.M.; Qamer, F.M.; Pengra, B.; Thau, D. Distribution and dynamics of mangrove forests of South Asia. *J. Environ. Manag.* **2015**, *148*, 101–111. [[CrossRef](#)]
35. Chen, B.; Xiao, X.; Li, X.; Pan, L.; Doughty, R.; Ma, J.; Giri, C. A mangrove forest map of China in 2015: Analysis of time series Landsat 7/8 and Sentinel-1A imagery in Google Earth Engine cloud computing platform. *ISPRS J. Photogramm. Remote Sens.* **2017**, *131*, 104–120. [[CrossRef](#)]
36. Hinton, G.E.; Osindero, S.; Teh, Y.W. A Fast Learning Algorithm for Deep Belief Nets. *Neural Comput.* **2006**, *18*, 1527–1554. [[CrossRef](#)] [[PubMed](#)]
37. Satyanarayana, B.; Mohamad, K.A.; Idris, I.F.; Husain, M.-L.; Dahdouh-Guebas, F. Assessment of mangrove vegetation based on remote sensing and ground-truth measurements at Tumpat, Kelantan Delta, East Coast of Peninsular Malaysia. *Int. J. Remote Sens.* **2011**, *32*, 1635–1650. [[CrossRef](#)]
38. Satyanarayana, B.; Koedam, N.; Smet, K.D.; Nitto, D.D.; Dahdouh-Guebas, F. Long-term mangrove forest development in Sri Lanka: Early predictions evaluated against outcomes using VHR remote sensing and VHR ground-truth data. *Mar. Ecol. Prog. Ser.* **2012**, *443*, 51–63. [[CrossRef](#)]
39. Leempoel, K.; Satyanarayana, B.; Bourgeois, C.; Zhang, J.; Chen, M.; Wang, J.; Dahdouh-Guebas, F. Dynamics in mangroves assessed by high-resolution and multi-temporal satellite data: A case study in Zhanjiang Mangrove National Nature Reserve (ZMNNR), P. R. China. *Biogeosciences* **2013**, *10*, 5681–5689. [[CrossRef](#)]
40. Chen, S.; Wang, H.; Xu, F.; Jin, Y.Q. Target Classification Using the Deep Convolutional Networks for SAR Images. *IEEE Trans. Geosci. Remote Sens.* **2016**, *54*, 4806–4817. [[CrossRef](#)]
41. Zhao, W.; Du, S. Spectral-spatial feature extraction for hyperspectral image classification: A dimension reduction and deep learning approach. *IEEE Trans. Geosci. Remote Sens.* **2016**, *54*, 4544–4554. [[CrossRef](#)]
42. Xu, Z.; Xu, X.; Wang, L.; Yang, R.; Pu, F. Deformable ConvNet with Aspect Ratio Constrained NMS for Object Detection in Remote Sensing Imagery. *Remote Sens.* **2017**, *9*, 1312. [[CrossRef](#)]
43. Krizhevsky, A.; Sutskever, I.; Hinton, G. *ImageNet Classification with Deep Convolutional Neural Networks*; NIPS. Curran Associates Inc.: Lake Tahoe, NV, USA, 2012.
44. Dubey, A.; Naik, N.; Parikh, D.; Raskar, R.; Hidalgo, C.A. Deep Learning the City: Quantifying Urban Perception at a Global Scale. In Proceedings of the European Conference on Computer Vision (ECCV), Amsterdam, Netherlands, 11–14 October 2016; Springer International Publishing: Cham, Switzerland, 2016.
45. Mohammadi, M.; Al-Fuqaha, A.; Guizani, M.; Oh, J.S. Semi-supervised Deep Reinforcement Learning in Support of IoT and Smart City Services. *IEEE Internet Things J.* **2017**, *5*, 624–635. [[CrossRef](#)]
46. Guo, Y.; Chen, E.; Guo, Y.; Li, Z.; Xu, K. Deep highway unit network for land cover type classification with GF-3 SAR imagery. In Proceedings of the 2017 SAR in Big Data Era: Models, Methods and Applications (BIGSARDATA), Beijing, China, 13–14 November 2017.
47. Guo, Y.; Chen, E.; Li, Z.; Li, Z.; Xu, K. Convolutional Highway Unit Network for Large-Scale Classification with GF-3 Dual-Pol Sar Data. In Proceedings of the IGARSS 2018—2018 IEEE International Geoscience and Remote Sensing Symposium, Valencia, Spain, 22–27 July 2018.
48. Yiming, C.; Yanbing, P.; Jianfei, G. *New Semantic Segmentation of Remote Sensing Image Based on Deep Learning*; Computer & Digital Engineering: Wuhan, China, 2019.
49. Liu, D.; Wen, B.; Jiao, J.; Xianming, L.; Zhangyang, W.; Thomas, S.H. Connecting Image Denoising and High-Level Vision Tasks via Deep Learning. *IEEE Trans. Image Process.* **2020**, *29*, 3695–3706. [[CrossRef](#)]
50. Cai, X.; Song, B.; Fang, Z. Exemplar based regular texture synthesis using LSTM. *Pattern Recognit. Lett.* **2019**, *128*, 226–230. [[CrossRef](#)]
51. Hu, F.; Li, L.; Zhang, Z.L.; Wang, J.Y.; Xu, X.F. Emphasizing Essential Words for Sentiment Classification Based on Recurrent Neural Networks. *J. Comput. Sci. Technol.* **2017**, *32*, 785–795. [[CrossRef](#)]

52. Guo, W.; Wu, R.; Chen, Y.; Zhu, X. Deep Learning Scene Recognition Method Based on Localization Enhancement. *Sensors* **2018**, *18*, 3376. [[CrossRef](#)] [[PubMed](#)]
53. Niu, Y.; Lu, Z.; Wen, J.R.; Tao, X.; Shih-Fu, C. Multi-Modal Multi-Scale Deep Learning for Large-Scale Image Annotation. *IEEE Trans. Image Process.* **2017**, *28*, 1720–1731. [[CrossRef](#)]
54. Zhang, L.; Zhang, L.; Du, B. Deep Learning for Remote Sensing Data: A Technical Tutorial on the State of the Art. *IEEE Geosci. Remote Sens. Mag.* **2016**, *4*, 22–40. [[CrossRef](#)]
55. Wichmann, A.; Agoub, A.; Schmidt, V.; Kada, M. RoofN3D: A Database for 3D Building Reconstruction with Deep Learning. *Photogramm. Eng. Remote Sens.* **2019**, *85*, 435–443. [[CrossRef](#)]
56. Pleoianu, A.I.; Stupariu, M.S.; Sandric, I.; Stupariu, I.; Drăgu, L. Individual Tree-Crown Detection and Species Classification in Very High-Resolution Remote Sensing Imagery Using a Deep Learning Ensemble Model. *Remote Sens.* **2020**, *12*, 2426. [[CrossRef](#)]
57. Lian, R.; Huang, L. DeepWindow: Sliding Window Based on Deep Learning for Road Extraction from Remote Sensing Images. *IEEE J. Sel. Top. Appl. Earth Obs. Remote Sens.* **2020**, *13*, 1905–1916. [[CrossRef](#)]
58. Faza, S.; Nababan, E.B.; Efendi, S.; Basyuni, M.; Rahmat, R.F. An initial study of deep learning for mangrove classification. *IOP Conf. Ser. Mater. Sci. Eng.* **2018**, *420*, 012093. [[CrossRef](#)]
59. Iovan, C.; Kulwicki, M.; Mermet, E. Deep Convolutional Neural Network for Mangrove Mapping. In Proceedings of the 2020 IEEE International Geoscience and Remote Sensing Symposium, Waikoloa, HI, USA, 19–24 July 2020.
60. Hinton, G.E.; Krizhevsky, A.; Wang, S.D. Transforming Auto-Encoders. In Proceedings of the Artificial Neural Networks & Machine Learning-ICANN-International Conference on Artificial Neural Networks, Lausanne, Switzerland, 11–14 September 2012; Springer: Berlin/Heidelberg, Germany, 2012.
61. Yang, X.; Li, X.; Ye, Y.; Lau, R.Y.K.; Huang, X. Road Detection and Centerline Extraction Via Deep Recurrent Convolutional Neural Network U-Net. *IEEE Trans. Geosci. Remote Sens.* **2019**, *57*, 7209–7220. [[CrossRef](#)]
62. Guo, Y.; Liao, J.; Shen, G. A Deep Learning Model with Capsules Embedded for High Resolution Image Classification. *IEEE J. Sel. Top. Appl. Earth Obs. Remote Sens.* **2020**, *14*, 214–223. [[CrossRef](#)]
63. Zhen, J.; Liao, J.; Shen, G. Mapping Mangrove Forests of Dongshaigang Nature Reserve in China Using Landsat 8 and Radarsat-2 Polarimetric SAR Data. *Sensors* **2018**, *18*, 4012. [[CrossRef](#)] [[PubMed](#)]
64. Thakkar, V.; Tewary, S.; Chakraborty, C. Batch Normalization in Convolutional Neural Networks—A comparative study with CIFAR-10 data. In Proceedings of the 2018 Fifth International Conference on Emerging Applications of Information Technology (EAIT), Kolkata, India, 12–13 January 2018.
65. Namozov, A.; Cho, Y.I. An Improvement for Medical Image Analysis Using Data Enhancement Techniques in Deep Learning. In Proceedings of the 2018 International Conference on Information and Communication Technology Robotics (ICT-ROBOT), Busan, Korea, 6–8 September 2018.
66. Bunting, P.; Rosenqvist, A.; Lucas, R.M.; Rebelo, L.M.; Hilarides, L.; Thomas, N.; Hardy, A.; Itoh, T.; Shimada, M.; Finlayson, C.M. The Global Mangrove Watch—A New 2010 Baseline of Mangrove Extent. *Remote Sens.* **2018**, *10*, 1669. [[CrossRef](#)]
67. Zhang, Z.; Liu, Q.; Wang, Y. Road Extraction by Deep Residual U-Net. *IEEE Geosci. Remote Sens. Lett.* **2017**, *15*, 749–753. [[CrossRef](#)]
68. Hemeleers, L.; Koedam, N.; Dahdouh-Guebas, F. World-wide mangrove distribution and degradation. In Proceedings of the Symposium African Botany, Brussels, Belgium, 27 March 2009; p. 86.
69. FAO. *The World's Mangroves 1980–2005*; FAO Forestry Paper; FAO: Rome, Italy, 2008; pp. 703–704.
70. Lv, T.; Zhou, X.; Liu, C.; Tao, Z.; Trisurat, Y. Data set of mangrove spatial distribution in Southeast Asia [DB/OL]. *Glob. Res. Data Publ. Repos.* **2015**. [[CrossRef](#)]
71. Li, C. *Remote Sensing Information Extraction and Spatial Evolution Mechanism of Mangrove*; Science Press: Beijing, China, 2013.
72. Zhang, H.; Li, D.; Wang, J.; Zhou, H.; Li, Y. Long time-series remote sensing analysis of the periodic cycle evolution of the inlets and ebb-tidal delta of Xincun Lagoon, Hainan Island, China. *ISPRS J. Photogramm. Remote Sens.* **2020**, *165*, 67–85. [[CrossRef](#)]
73. Lucas, R.; Kerchove, R.V.D.; Otero, V.; Lagomasino, D.; Dahdouh-Guebas, F. Structural characterisation of mangrove forests achieved through combining multiple sources of remote sensing data. *Remote Sens. Environ.* **2020**, *237*, 111543. [[CrossRef](#)]
74. Ma, C.; Ai, B.; Zhao, J. Change Detection of Mangrove Forests in Coastal Guangdong during the Past Three Decades Based on Remote Sensing Data. *Remote Sens.* **2019**, *11*, 921. [[CrossRef](#)]
75. Richards, D.R.; Friess, D.A. Rates and drivers of mangrove deforestation in Southeast Asia, 2000–2012. *Proc. Natl. Acad. Sci. USA* **2015**, *113*, 344–349. [[CrossRef](#)]
76. Hao, L.; Yi, M.A.; Guang-Bo, R. Remote sensing monitoring of the mangrove forests resources of Kra Isthmus in Thailand. *Mar. Environ. Sci.* **2016**, *35*, 725–731.
77. Estoque, R.C.; Myint, S.W.; Chuyuan, W.; Xu, X.; Huang, H. Assessing environmental impacts and change in Myanmar's mangrove ecosystem service value due to deforestation (2000–2014). *Glob. Chang. Biol.* **2018**, *24*, 5391–5410. [[CrossRef](#)]
78. Wu, P.; Zhang, J.; Yi, M.A.; Ren, G.B. Remote Sensing Monitoring and Analysis of the Dynamics of Mangrove Resources in Thailand from 1980 to 2015. *Adv. Mar. Sci.* **2018**, *36*, 86–96.
79. Ilman, M.; Dargusch, P.; Dart, P.; Onrizal. A historical analysis of the drivers of loss and degradation of Indonesia's mangroves. *Land Use Policy* **2016**, *54*, 448–459. [[CrossRef](#)]
80. Brown, B.; Yuniat, W.; Ahmad, R.; Soulsby, I. *Observations of Natural Recruitment and Human Attempts at Mangrove Rehabilitation after Seismic (Tsunami and Earthquake) Events in Simeulue Island and Singkil Lagoon, Aceh, Indonesia*; Springer International Publishing: Cham, Switzerland, 2015.

81. Ramakrishnan, R.; Gladston, Y.; Kumar, N.L.; Rajput, P.; Rajawat, A.S. Impact of 2004 co-seismic coastal uplift on the mangrove cover along the North Andaman Islands. *Reg. Environ. Chang.* **2020**, *20*, 6. [[CrossRef](#)]
82. Luo, Jia, H.; Wenyu, L.; Bing, X. Monitoring mangrove forest change in China from 1990 to 2015 using Landsat-derived spectral-temporal variability metrics. *Int. J. Appl. Earth Obs. Geoinf.* **2018**, *73*, 88–98.
83. Kumar, R.C.S.; Kumar, G.T.R.; Renjith, K.R.; Manju, K.R.; Chandramohanakumar, M.N.A. Spatial Variability and Contamination of Heavy Metals in the Inter-Tidal Systems of a Tropical Environment. *Int. J. Environ. Res.* **2010**, *4*, 691–700.
84. Saravanan, S.; Jegankumar, R.; Selvaraj, A.; Jacinth, J.J.; Parthasarathy, K.S.S. Utility of Landsat Data for Assessing Mangrove Degradation in Muthupet Lagoon, South India. In *Coastal Zone Management*; Elsevier: Amsterdam, The Netherlands, 2019; pp. 471–484.
85. Salik, K. *Impact of Climate Change on Mangrove Ecosystem in South Asia*; LAP LAMBERT Academic Publishing: Saarbrücken, Germany, 2016.
86. Kamboj, R.D.; Das, L. The Dynamics of Mangrove Cover in India: Based on Assessment done by Forest Survey of India from 1987 to 2017. *Indian For.* **2019**, *145*, 607–613.
87. Quader, M.A.; Agrawal, S.; Kervyn, M. Multi-decadal land cover evolution in the Sundarban, the largest mangrove forest in the world. *Ocean Coast. Manag.* **2017**, *139*, 113–124. [[CrossRef](#)]
88. Little, D.I. Mangrove Restoration and Mitigation after Oil Spills and Development Projects in East Africa and the Middle East. In *Threats to Mangrove Forests*; Springer: Cham, Switzerland, 2018.
89. Murray, N.J.; Phinn, S.R.; Dewitt, M.; Ferrari, R.; Fuller, R.A. The global distribution and trajectory of tidal flats. *Nature* **2019**, *565*, 222–225. [[CrossRef](#)]
90. Saber, G.; Sina, S.M.; Amir, R.; Christos, A.D.; Abolfazl, N. Phytomanagement of trace metals in mangrove sediments of Hormozgan, Iran, using gray mangrove (*Avicennia marina*). *Environ. Sci. Pollut. Res.* **2018**, *25*, 28195–28205.
91. Mafi, D. Adverse effects of climate change on mangroves and requisite approaches to increase resistance of these ecosystems. In Proceedings of the 2nd International Conference & 3rd National Conference on New Technologies Application in Engineering, Mashhad, Iran, 25 February 2016.
92. Jerath, M.; Bhat, M.; Rivera-Monroy, V.H.; Castaneda-Moya, E.; Simard, M.; Twilley, R.R. The role of economic, policy, and ecological factors in estimating the value of carbon stocks in Everglades mangrove forests, South Florida, USA. *Environ. Sci. Policy* **2016**, *66*, 160–169. [[CrossRef](#)]